

## Research Paper

# Unsteady Flow Patterns Between Two Egg-Carton Corrugated Plates

Benjamin GIRÓN-PALOMARES<sup>1)</sup>, Abel HERNÁNDEZ-GUERRERO<sup>2)</sup>,  
Ricardo ROMERO-MÉNDEZ<sup>3)</sup>, Qiang HE<sup>4)</sup>\*

<sup>1)</sup> *Engineering Training Center  
Anyang Institute of Technology  
Anyang, 455000, China  
e-mail: tiny\_ikari@yahoo.com.mx*

<sup>2)</sup> *Mechanical Engineering Department  
University of Guanajuato  
Salamanca, Gto, 36885, Mexico  
e-mail: abel@ugto.mx*

<sup>3)</sup> *Engineering Faculty  
Autonomous University of San Luis Potosi  
Av. Dr. Manuel Nava 8, Zona Universitaria, San Luis Potosí, SLP 78290, Mexico  
e-mail: rromerom@uaslp.mx*

<sup>4)</sup> *Department of Mechanical Engineering  
Anyang Institute of Technology  
Anyang, 455000, China*

\*Corresponding Author e-mail: 389975927@qq.com

Unsteady analyses of the flow between two egg-carton corrugated plates were performed. Geometry effects on the flow were as follows: “closed recirculations” shrank downstream the channel and became “open recirculations”. For the 180° egg-carton plates, recirculations were  $z$ -symmetric to the channel center. Reynolds number increments favored recirculation growth and flow detachment. Transient development effects were as follows: the steady state was reached faster in waves closer to the channel entrance. As time advanced, spatial flow development advanced toward the channel outlet, and  $y$ -concave geometries inhibited fluid detachment and steady state achievement. Consequences of the geometry on the transient development of the flow were as follows: the recirculations appeared at larger times, they were smaller, and became “open recirculations” closer to the channel inlet for the 0° model, and the 0° model flow reached a steady state faster. Finally, no clear evidence of unsteady features called “rolling vortices” was observed. Such unsteady features might be a consequence of small unavoidable experimental uncertainties creating a pulsating flow.

**Key words:** egg-carton corrugated plates; unsteady flow pattern; 3D chaotic flow; numerical analysis; recirculation; rolling vortices; pulsating flow.

## NOTATIONS

- $A$  – amplitude, m,  
 $\mathbf{g}$  – gravitational acceleration,  $\text{m/s}^2$ ,  
 $H_{\text{avg}}$  – the average distance between corrugated plates, m,  
 $P$  – pressure, Pa,  
 $P_1, \dots, P_6$  – monitored points in the secondary flow region,  
 $P_i, P_o$  – monitored points close to the inlet and outlet,  
 $\text{Re}$  – Reynolds number, dimensionless,  
 $R_{st}$  – detachment point  $x$ -location, m,  
 $R_L$  – recirculation  $x$ -length, m,  
 $t$  – time, s,  
 $\mathbf{v}$  – velocity,  $\text{m/s}$ ,  
 $x, y, z$  – Cartesian coordinate system, m.

**Greek symbols**

- $\mu$  – dynamic viscosity,  $\text{Pa} \cdot \text{s}$ ,  
 $\Lambda$  – wavelength, m,  
 $\rho$  – density,  $\text{kg/m}^3$ ,  
 $\phi$  – scalar variable,  
 $\delta$  – hydrodynamic boundary layer thickness.

**Subscripts and superscripts**

- $x, y, z$  – variable acting on the  $x, y,$  or  $z$  direction.

## 1. INTRODUCTION

Multiple investigations have been conducted to improve mixing at low Reynolds numbers by modifying the geometry of the walls and/or the characteristics of the main flow [1–7] in heat exchangers applications and microfluidic applications involving chemical reactions. The improvement in mixing leads to a better transfer of thermal energy. In particular, several researchers [2, 7–12] reduced thermal resistance close to the plates of the heat exchangers by using corrugated plates (1-D corrugations in the direction of the main flow) instead of flat plates. Such corrugations generate recirculations and better mixing. However, they also produce naturally higher pressure drops. Searching for better mixing, few researchers [13, 14] have added corrugations not only in the streamwise but also in the spanwise directions of the flow, generating an egg-carton corrugated plate. By studying 2-D fluid particles pathlines of the flow between two egg-carton corrugated plates, SAWYERS *et al.* [14] observed fluid particles leaving the recirculation and joining the main flow, while GIRÓN-PALOMARES *et al.* [13] observed open recirculations and rolling vortices allowing interaction be-

tween the secondary and main flow. Such interactions between the secondary flow and the main flow, reported in [13, 14], improve the mixing of the fluid.

Theoretical investigations [14] on egg-carton corrugated plates usually make several assumptions (steady state, full development, and periodic flow), while the experimental counterpart [13] keeps the flow between egg-carton corrugated plates closer to reality. Several experimental investigations [8, 9, 13, 15] have reported possible unsteady flow features (open recirculations, rolling vortices, and macroscopic mixing) in the flow between two corrugated plates. However, it is not completely clear if such flow features are effects of the plate geometry or consequences of experimental conditions uncertainties (unavoidable small variations on the flow velocity creating a pulsating flow or a transient flow that has not achieved a steady state). In order to verify if such unsteady features are a consequence of unsteady artifacts, GIRÓN-PALOMARES *et al.* [16] performed a detailed numerical steady analysis of a long egg-carton corrugated channel (i.e., a corrugated channel with corrugations not only in the streamwise but also in the spanwise directions of the flow) avoiding the fully developed and periodic flow considerations. The authors [16] observed not only open recirculations and macroscopic mixing, but also a complex 3-D behavior of the fluid. These observations confirmed the egg-carton corrugated plate geometry effects (open recirculations, macroscopic mixing and 3-D behavior) on the flow and ruled out unsteady artifacts as the cause of such flow features observed in experimental works. Nevertheless, no rolling vortices were observed and such flow feature could be a consequence of unwanted experimentally introduced unsteadiness. Rolling vortices are unsteady features that improve the transport of fluid and therefore mixing. In consequence, this additional mixing feature will locate egg-carton channels as the leading corrugated channels to improve mixing in the laminar regime. Nevertheless, these rolling vortices could result from unavoidable small variations of the flow velocity creating a pulsating flow. Pulsating flows have been used by several researchers [1, 3, 5, 6] to improve mixing and heat transfer. A detailed unsteady analysis of the flow between two egg-carton corrugated plates was performed in this research to explore such possibility. The unsteady model was built based on the steady model developed in [16] (a model exhibiting local and global convergence, as well as spatial mesh size independence), and it was corroborated to have temporal mesh size independence. As in [16], two phase angles ( $180^\circ$  and  $0^\circ$ ) between the top and bottom plates were investigated, and they were referred to as the  $180^\circ$  model and the  $0^\circ$  model, respectively. To observe the differences in the flow pattern as turbulent regimes are approached, Reynolds numbers from 100 to 600 were considered. It is imperative to examine if egg-carton corrugated plates generate rolling vortices, because this phenomenon will make egg-carton corrugated plates as the leading corrugated channels to improve mixing in the laminar regime.

## 2. METHODOLOGY

The procedure used in this research work was as follows:

- 1) Develop unsteady hydrodynamic numerical models of two egg-carton plates with the geometrical characteristics and operating conditions of a previously developed spatial mesh size independent model [16].
- 2) Solve the unsteady models for four different time steps, three different Reynolds numbers, and confirm local as well as global convergence for each model.
- 3) Compare the different time-step models to confirm that further reduction of the time step is not necessary (i.e., temporal mesh size independence has been obtained).
- 4) Verify that the flow patterns obtained at a very long time agree with the steady state results obtained in [16].
- 5) Analyze and discuss the development of the flow pattern in space and time for the results obtained from the numerical models exhibiting spatial and temporal mesh size independence.

The characteristics of the unsteady hydrodynamic numerical models and the numerical solution procedure are described in Subsec. 2.1. Subsection 2.2 shows the rigorous methodology used to develop numerical models that exhibit global convergence, local convergence, as well as spatial and temporal mesh-size independence. Steps 2 to 4 of the procedure shown above are discussed in Sec. 3. Finally, step 5 is described in Sec. 4.

### 2.1. Governing equations, discretization and solution procedure

Schematic views of the heat exchanger plate geometries studied in this research are shown in Figs 1 and 2. The location of a point at the top corrugated plate can be described by the following equation:

$$(2.1) \quad z = \frac{H_{\text{avg}}}{2} + A_x \cos\left(\frac{2\pi x}{\Lambda_x}\right) + A_y \cos\left(\frac{2\pi y}{\Lambda_y}\right),$$

where  $x$ ,  $y$ , and  $z$  are the Cartesian coordinates,  $\Lambda_x$  is the wavelength in the  $x$ -direction,  $A_x$  is the amplitude of the wave in the  $x$ -direction,  $\Lambda_y$  is the wavelength in the  $y$ -direction,  $A_y$  is the amplitude of the wave in the  $y$ -direction, and  $H_{\text{avg}}$  is the average distance between plates (see Figs 1 and 2). A similar expression can be obtained for the bottom plate.

The computational domain was considered as fluid bounded by walls, except for the inlet and the outlet. The top and bottom walls were the corrugated plates with a  $180^\circ$  or  $0^\circ$  phase angle (applied in both  $x$  and  $y$  directions), while the

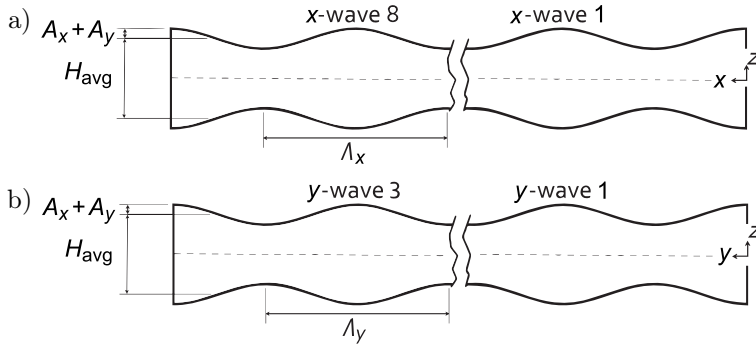


FIG. 1. Schematic view of the egg carton plates with a  $180^\circ$  phase angle: a) lateral view (the main flow direction is from right to left) and b) frontal view.  $H_{\text{avg}} = 30$  mm,  $A_x = 4.5$  mm,  $A_y = 3$  mm,  $\Lambda_x = 83.34$  mm, and  $\Lambda_y = 76.25$  mm.

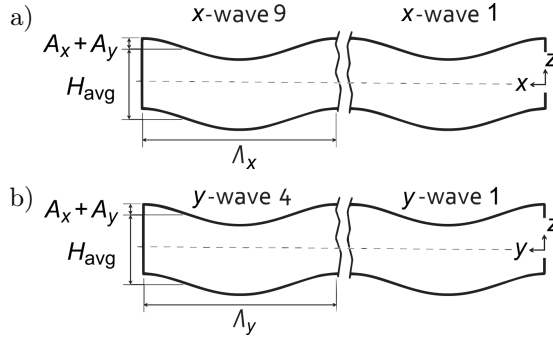


FIG. 2. Schematic view of the egg carton plates with a  $0^\circ$  phase angle: a) lateral view (the main flow direction is from right to left) and b) frontal view.  $H_{\text{avg}} = 30$  mm,  $A_x = 4.5$  mm,  $A_y = 3$  mm,  $\Lambda_x = 83.34$  mm, and  $\Lambda_y = 76.25$  mm.

side walls were considered to be flat and parallel to the  $xz$ -plane. The governing equations for the flow in the computational domain are the continuity and Navier-Stokes equations. If the fluid is considered Newtonian, incompressible, and with constant viscosity, the governing equations take the following forms:

$$\frac{\partial v_x}{\partial x} + \frac{\partial v_y}{\partial y} + \frac{\partial v_z}{\partial z} = 0,$$

$$(2.2) \quad \rho \left( \frac{\partial v_x}{\partial t} + v_x \frac{\partial v_x}{\partial x} + v_y \frac{\partial v_x}{\partial y} + v_z \frac{\partial v_x}{\partial z} \right) = \rho g_x - \frac{\partial P}{\partial x} + \mu \left( \frac{\partial^2 v_x}{\partial x^2} + \frac{\partial^2 v_x}{\partial y^2} + \frac{\partial^2 v_x}{\partial z^2} \right),$$

$$\rho \left( \frac{\partial v_y}{\partial t} + v_x \frac{\partial v_y}{\partial x} + v_y \frac{\partial v_y}{\partial y} + v_z \frac{\partial v_y}{\partial z} \right) = \rho g_y - \frac{\partial P}{\partial y} + \mu \left( \frac{\partial^2 v_y}{\partial x^2} + \frac{\partial^2 v_y}{\partial y^2} + \frac{\partial^2 v_y}{\partial z^2} \right),$$

$$\rho \left( \frac{\partial v_z}{\partial t} + v_x \frac{\partial v_z}{\partial x} + v_y \frac{\partial v_z}{\partial y} + v_z \frac{\partial v_z}{\partial z} \right) = \rho g_z - \frac{\partial P}{\partial z} + \mu \left( \frac{\partial^2 v_z}{\partial x^2} + \frac{\partial^2 v_z}{\partial y^2} + \frac{\partial^2 v_z}{\partial z^2} \right),$$

where  $x$ ,  $y$ , and  $z$  are the Cartesian coordinates,  $\mathbf{v}$  is the velocity,  $P$  is the pressure,  $\mathbf{g}$  is the gravitational acceleration,  $t$  is the time,  $\rho$  is the density of the fluid,  $\mu$  is the dynamic viscosity, and the subscript  $x$ ,  $y$  or  $z$  indicates a scalar component of a vectorial variable acting on the  $x$ ,  $y$  or  $z$  direction.

The boundary conditions used to solve the governing equations were as follows: non-slip boundary conditions for all the walls in the computational domain, an inflow boundary condition at the inlet of the channel with a uniform velocity profile, and a pressure outlet boundary condition at the exit of the channel (this boundary condition accounts for sudden expansions or divergent geometries by allowing backflow and flow separation). Because the outlet and the surface of the corrugated plate are mutually perpendicular, the backflow was considered to be perpendicular to the outlet boundary. In this way, the outlet flow variables were determined from the interior. The magnitude of the velocity at the inlet was determined according to the Reynolds numbers studied. In agreement with a previous steady analysis [16] of these plates, the static pressure (gauge pressure) was applied as 0 Pa. These boundary conditions were applied for any time larger than zero.

The computational solution of the governing equations was obtained by implementing a finite volume method in ANSYS FLUENT. First, the spatial computational domain was divided into discrete control volumes using a computational grid (mesh). A uniform mapped mesh with more than 10 million finite volumes, providing high-quality cells, was used (see [16] for a detailed description). Next, Fluent created a system of algebraic equations by applying and integrating the conservation governing equations over every single discrete volume. The system of algebraic equations was linearized and solved by using a Fluent pressure-based solver. For the transient analysis, the *pressure-implicit with splitting of operators* (PISO) [17, 18] scheme is a pressure-velocity coupling scheme that is more efficient than the SIMPLE (i.e., a segregated algorithm [19]) scheme. The COUPLED algorithm [20] is usually more stable and faster than the SIMPLE or PISO algorithms but requires a computer with larger RAM. According to [16], the COUPLED algorithm was able to obtain converged steady solutions for high Reynolds numbers and number of cells in the same mesh model of the steady flow between the egg-carton corrugated plates. Therefore, the COUPLED algorithm was chosen as the first option to obtain the unsteady flow solution. When the solution residuals presented unstable or stalling convergence behavior, the solution algorithm was changed to the PISO algorithm. The under-relaxation factors (commercial code default optimum values) were used for velocity, pressure, conservation equations, density, and body forces in order to avoid instabilities or divergence of the solution. Such optimum values were reduced when needed (i.e., when residuals stalling, divergence or instabilities were observed). On the other hand, interpolation procedures were used to obtain the value of the

solution variable at the faces of the cell (the pressure-based solver obtains the solutions only at the center of the cells). A second-order Fluent upwind interpolation scheme was used for velocities. In the case of the pressure, the Fluent PRESTO! interpolation scheme [19, 21] was used. Models presenting swirling or high boundary curvatures work well with PRESTO! interpolation schemes. These spatial discretization and solution procedures were applied to every unsteady state numerical model generated in this research.

The temporal term on the governing equations was discretized using backward finite differences. Therefore, the following discretized version of the momentum governing equations should be solved:

$$(2.3) \quad \frac{3\phi^{n+1} - 4\phi^n + \phi^{n-1}}{2\Delta t} = F(\phi^{n+1}), \quad \text{second order temporal discretization,}$$

where  $n$  indicates the value of a particular variable at the  $n$ -time,  $\Delta t$  is the time increment,  $\phi$  is the scalar variable ( $v_x$ ,  $v_y$ , or  $v_z$ ), and  $F(\phi^{n+1})$  is a function involving any spatial discretization performed. This equation was implicitly discretized (i.e.,  $F(\phi)$  was evaluated at the unknown state  $n + 1$ ), and its solution was unconditionally stable with respect to the time increment size. The solution was obtained for every successive time step by an iterative solution method. At  $t = 0$ , it was considered that the fluid between the corrugated plates was at rest. It is important to remark that any compressibility effects in the fluid were neglected for every temporal solution determined.

## 2.2. Numerical models development procedure

The strict procedure to develop the numerical models was as follows:

- 1) Four computational fluid dynamics (CFD) models with different temporal mesh sizes were generated by using a previously developed model exhibiting spatial mesh size independence [16]. The time steps were selected in such a way that consecutive time steps have a decreasing ratio of 0.5. These four models are evaluated to ensure that the solutions are not affected by further reduction of the time step.
- 2) A reduction of six orders of magnitude in the scale residuals was considered for convergence. Additionally, the scalar velocities of points located at different regions of interest were observed to ensure local convergence (see Fig. 3). Such regions were chosen as the recirculation zones in  $x$ -wave 8 (points  $P_1$  to  $P_6$ ) and main flow areas (points  $P_i$  and  $P_o$ ). The comparison of the velocity variation in these regions among the different numerical models allows to study a temporal grid size independence. All of the points were studied in three different  $xz$ -planes located at  $y = 1A_y$ ,  $2A_y$ , and  $3A_y$ . Points  $P_i$  and  $P_o$  were located streamwise at  $x = 1A_x$  and  $x = 8A_x$  while

keeping a  $z$ -equidistant coordinate from the top and bottom plates. The  $z$  and  $x$ -locations for  $P_1$  to  $P_6$  can be observed in Fig. 3.

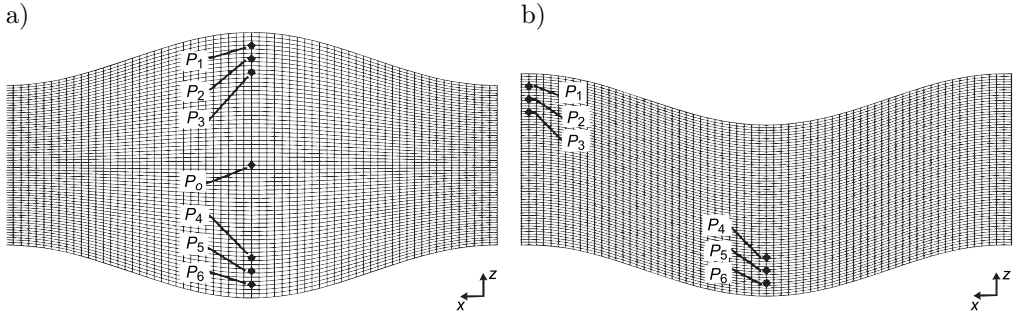


FIG. 3. Location of points monitored for the mesh size independence study on  $x$ -wave 8 and  $2\Delta_y$   $xz$ -plane for: a)  $180^\circ$  model, and b)  $0^\circ$  model.

The temporal grid size-independent model was used to study the flow pattern between the two heat exchanger plates as the time increased for different Reynolds numbers. Subsequently, the numerical model flow pattern was compared with the flow patterns obtained in previous experimental [13] and numerical studies [16]. It is important to mention that a temporal grid size independence study was performed for every Reynolds number considered (Reynolds number defined as a function of the uniform inlet velocity and the average distance between plates,  $H_{\text{avg}}$ ). Details on the results of the mesh size independence study as well as the numerical flow patterns development are given in Sec. 3.

### 3. RESULTS AND DISCUSSION

This section discusses the temporal size independence study results and the flow pattern behavior as the fluid travels downstream and the time progresses. As mentioned in Subsec. 2.1, the solver, interpolation schemes and relaxation factors were varied in order to obtain convergence. Usually and without considering a phase angle, the COUPLED algorithm with a second-order interpolation upwind scheme, a second-order implicit temporal discretization, average flow Courant number (120), and optimum relaxation factors (0.75 for pressure and 0.75 for momentum) worked well. However, for a Reynolds number of 600, a time step of 0.25 s and a  $180^\circ$  phase angle, only the PISO algorithm with a second-order interpolation upwind scheme, a second-order implicit temporal discretization, and relaxation factors of 0.3 for pressure and 0.75 for momentum was able to achieve convergence for every time step a solution was determined. The numerical study was performed for three Reynolds numbers (200, 400, and 600). For the sake of brevity, only the results for 600 are presented, but the re-

sults for the other Reynolds numbers are quite similar. Increments of Reynolds number were found to favor recirculation growth and early flow detachment; these dimensional effects in the recirculations of the Reynolds number are in line with previous experimental [13] and numerical investigations [16]. A very detailed analysis of the Reynolds number effects on the recirculations spatial behavior (spatial flow development) is presented in [16]. In the case of temporal flow development, Reynolds number increments increased the time needed to reach a steady state, but the behavior of the flow to achieve a fully temporal flow development (steady state) was the same regardless of Reynolds number. The results are divided into the  $180^\circ$  and  $0^\circ$  models results. A spatial size independence study was not performed. However, the spatial division of the model was chosen according to a previous spatial grid size independence study performed in the same geometrical model [16]. A finite element model with around ten million cells showed spatial mesh size independence. Accordingly, the length, the width, and the distance between the top and bottom of the corrugated plates were divided into 594, 264, and 64 segments. This technique produced a uniform mapped mesh providing high-quality cells. The unsteady results obtained in this work were compared with the steady-state analysis results. These steady state results are identical to those obtained in [16]. Therefore, this data is marked as “SS [16]” in any plot or graphic representation including such steady state results.

### *3.1. Transient flow pattern: $180^\circ$ model*

Figure 4a shows the converged scale residuals for a transient analysis performed for a total elapsed time of 93.25 s (as subsequently explained, the steady state has been well established at such time). 178 unsteady solutions were obtained using a time increment of 0.25 s for the first 157 solutions, 0.5 s for the next 4 solutions, 2 s for the next 8 solutions, and 4 s for the final 9 solutions. The continuity and velocity residuals were required to reach a value in the order of  $10^{-6}$  to consider the achievement of global convergence. Every time a solution was determined for a particular time, the scale residuals increased to a high initial value that kept reducing until convergence was achieved (i.e., a value in the order of  $10^{-6}$  was reached). The local convergence was verified for each temporal solution in the selected locations of the channel shown in Fig. 3a. For brevity's sake, only the local convergence plots for 29.25 s are shown in Figs 4b to 4d. In these figures, it can be seen how the local velocities reached a practically constant value (the absolute percentage of change between consecutive iterative velocities in the horizontal line region was determined to be well below 0.1%) for a considerable amount of iterations (i.e., local convergence has been achieved).

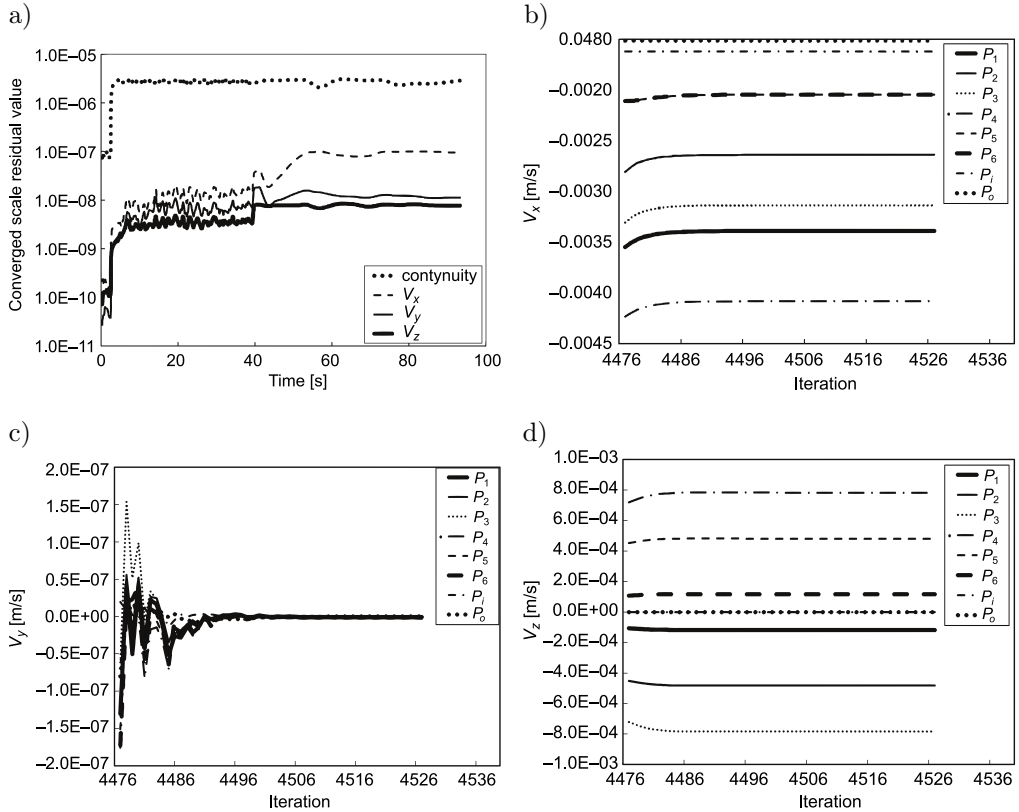


FIG. 4. Convergence study for: a) global convergence, b)  $V_x$  local convergence, c)  $V_y$  local convergence, and d)  $V_z$  local convergence.  $2\lambda_y$   $xz$ -plane and  $180^\circ$  model. Local convergence is shown for 29.25 s.

After proving global and local spatial convergence, a temporal size independence study was performed by considering four different time steps (0.25, 0.5, 1, and 2 s). The local velocities obtained for selected locations after 2 s are compared and shown in Fig. 5. From this figure, it can be observed that the difference among the converged velocities is not significant. Moreover, the velocity difference between those velocities for the first two time steps (0.25 and 0.5 s) is always the smallest. If percentages of difference were determined among the converged total velocities for consecutive time steps, maximum percentages of difference around 1.8% would be achieved between 0.25 and 0.5 s time steps. Therefore, it is safe to infer that converged velocities for time steps below 0.25 s will show no significant differences with those determined for a time step of 0.25 s. According to this, several solutions were obtained for a time step of 0.25 s until no significant differences were observed on the converged solution among consecutive solutions (i.e., until the steady state was achieved). For the few several starting solutions, a time step of 0.25 s was used, but it was gradually increased

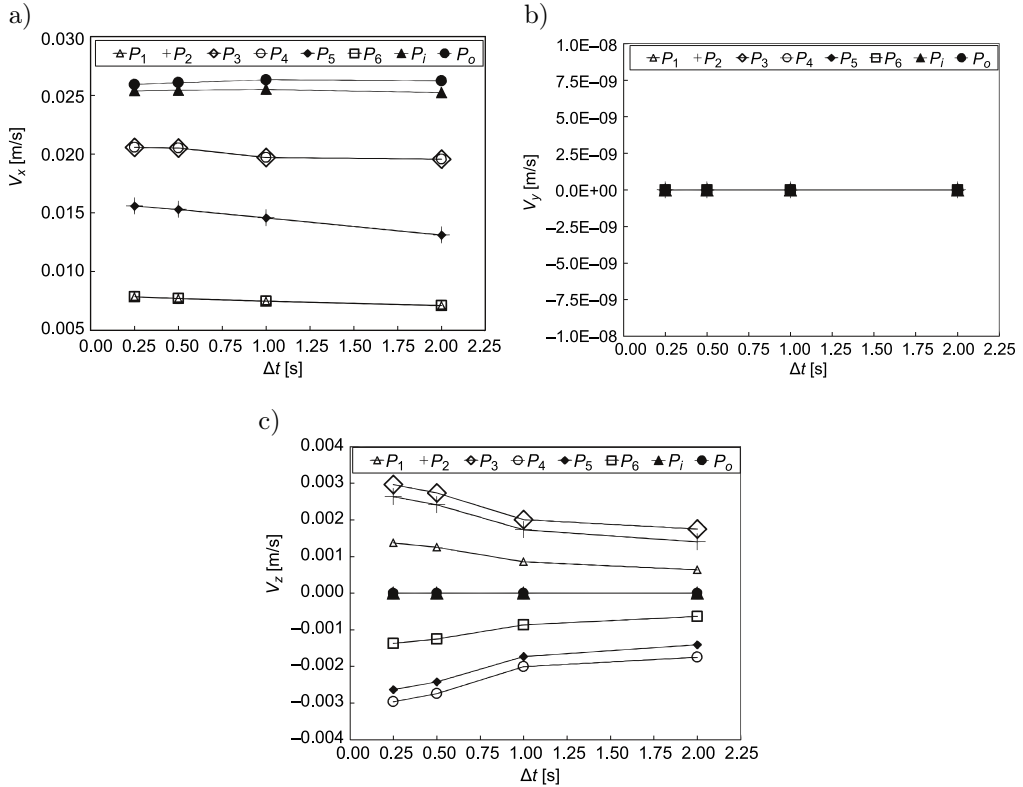


FIG. 5. Temporal size independence study for: a)  $V_x$ , b)  $V_y$ , and c)  $V_z$ ;  $2A_y$   $xz$ -plane and  $180^\circ$  model.

after a quasi-steady state was observed in order to entirely confirm a steady state at much longer times.

Figure 6 shows a few chosen path lines exemplifying the evolution of the recirculation formation as time proceeds. At early times (observe path lines for 1.25 s), it can be observed that the detachment point appears relatively far from the  $x$ -wave entrance, the reattachment point starts relatively close to the entrance of the next wave, and the size of the recirculation is quite small. At moderate times (observe path lines for 4.25 s), the detachment point is closer to the  $x$ -wave inlet, the reattachment point is quite far from the  $x$ -wave inlet, and the size of the recirculation is considerably larger and closer to the main flow. As time further advances, the detachment point keeps moving closer to the  $x$ -wave inlet, the reattachment point keeps advancing farther from the  $x$ -wave inlet, and the size of the recirculation keeps growing. Of course, these changes of the geometry of the recirculation reduce gradually until no changes are observed (i.e., steady state has been reached). The steady state is reached faster at  $x$ -waves closer to the inlet ( $x$ -wave 1 reached it around 7 s,  $x$ -wave 5 reached

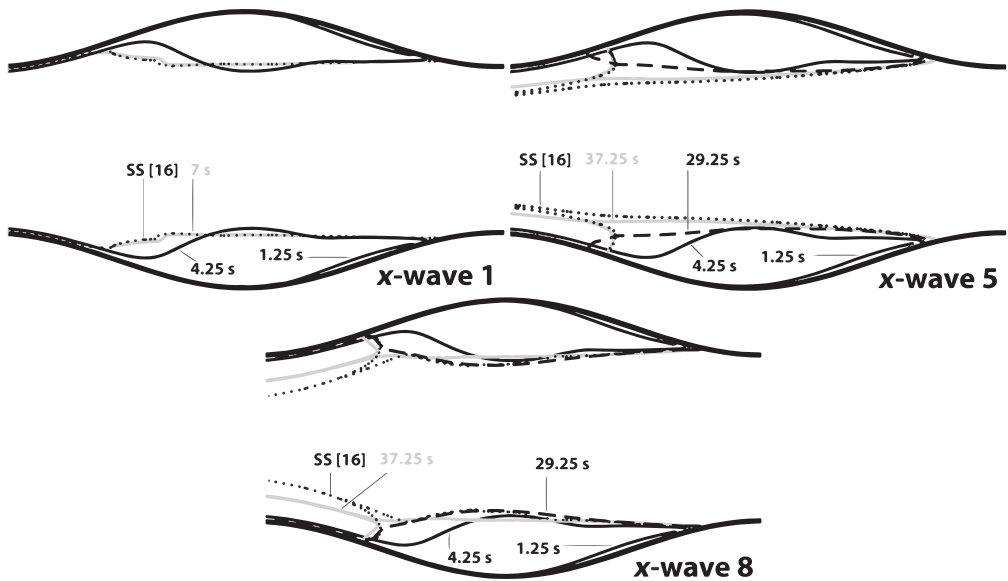


FIG. 6. Path lines showing the recirculation behavior as the fluid progresses downstream and time advances;  $2\Lambda_y$   $xz$ -plane and  $180^\circ$ .

it around 37.25 s, and  $x$ -wave 8 reached it after 37.25 s). At long enough times and  $x$ -waves numbers above wave 1, the fluid detaching from the wall does not reattach anymore and incorporates to the main flow (“open recirculations” are being formed), while the reattachment point is a point at which fluid incorporates from other planes and follows a downstream path (joining the main flow) or an upstream path (forming part of the “open recirculation”). Such appearances of these “open recirculations” as the flow approaches the channel outlet were well documented in [16] in the complete steady state analysis of such corrugated plates. This growing interaction between the secondary flow and the main flow, as the channel outlet is approached and as time advances, is a direct consequence of the flow developing in space and time.

Figures 7 to 9 show the  $x$ -velocity profiles at different channel locations for selected times (these locations are at the center of different  $x$ -waves). After the curves achieved a quasi-steady state, the temporal parametric curves are shown as solid lines. This procedure was used in all the parametric plots presented in this research to clearly show steady state achievement. By comparing  $x$ -velocity profiles at different channel locations, it can be observed that the walls affect more the channel center as the  $x$ -wave increases (i.e., spatial flow development). By comparing  $x$ -velocity profiles over time for a particular  $x$ -wave, it can be seen that the walls affect more and more the channel center as time progresses (i.e., temporal flow development). Of course, full development will be reached at long enough times and bigger lengths. Although spatial flow development cannot be

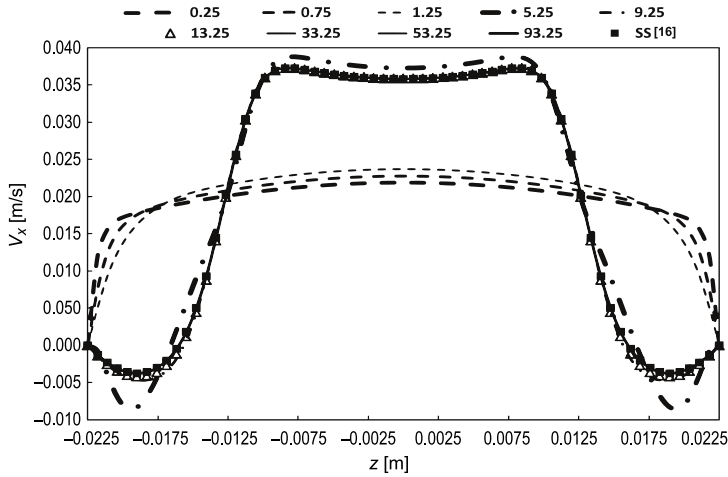


FIG. 7.  $V_x$  velocity profile as function of time for  $x = 1A_x$  and  $y = 2A_y$ ;  $Re = 600$ ,  $2A_y$   $xz$ -plane and  $180^\circ$  model.

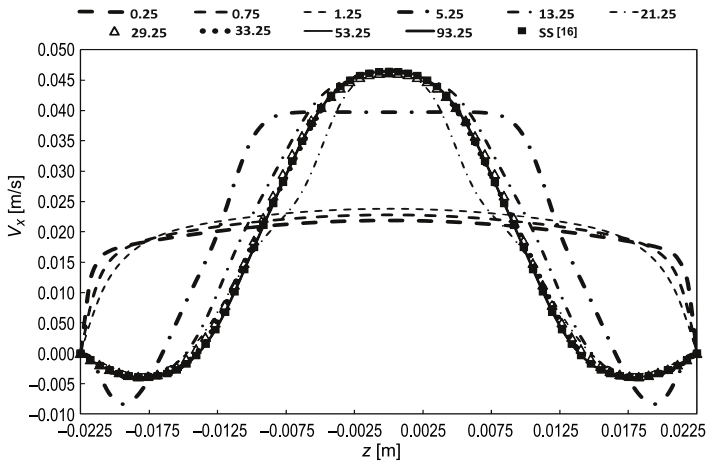


FIG. 8.  $V_x$  velocity profile as function of time for  $x = 5A_x$  and  $y = 2A_y$ ;  $Re = 600$ ,  $2A_y$   $xz$ -plane and  $180^\circ$  model.

completely achieved (the channel is periodically diverging and converging), temporal flow development was fully achieved. As observed in Figs 7 to 9, temporal flow development (steady state) has been reached at 13.25 s, 29.25 s, and 41.25 s for  $x$ -waves 1, 5, and 8, respectively, confirming that the steady state is reached faster at  $x$ -waves closer to the channel entrance. This behavior was observed in other locations of the  $x$ -waves. For example, Fig. 10 shows the  $x$ -velocity profile over time for the entrance of  $x$ -wave 8. From this figure, it can be seen how the velocity profile reaches the steady state at around 41.25 s. The difference

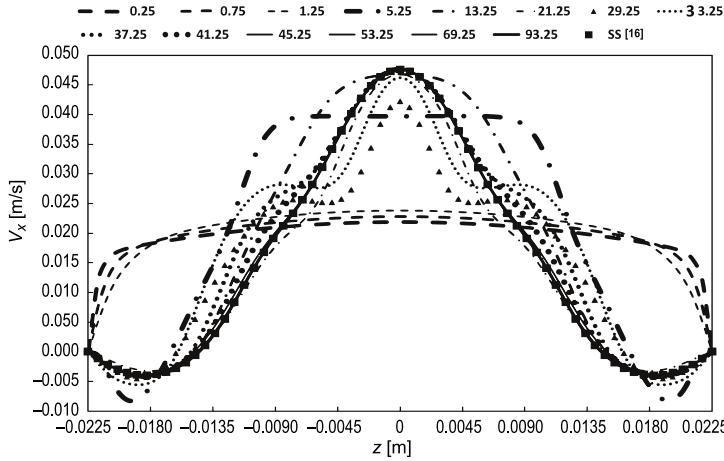


FIG. 9.  $V_x$  velocity profile as function of time for  $x = 8\Lambda_x$  and  $y = 2\Lambda_y$ ;  $Re = 600$ ,  $2\Lambda_y$   $xz$ -plane and  $180^\circ$  model.

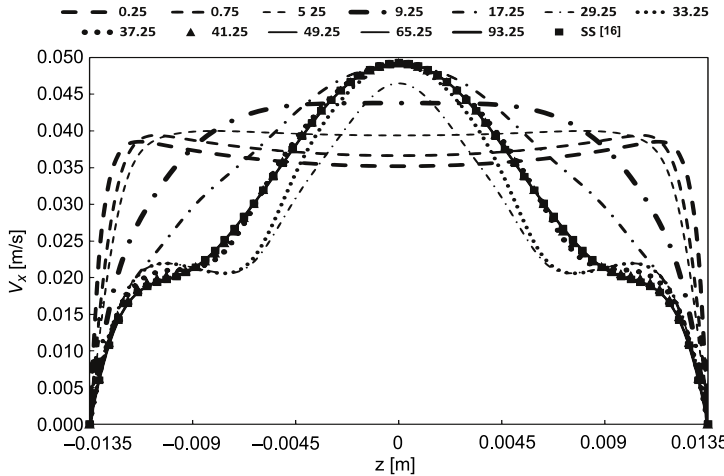


FIG. 10.  $V_x$  velocity profile as function of time for  $x = 7.5\Lambda_x$  and  $y = 2\Lambda_y$ ;  $Re = 600$ ,  $2\Lambda_y$   $xz$ -plane and  $180^\circ$  model.

with the  $x$ -velocity profile at the center of the  $x$ -waves is the lack of reversed flow promoted by the converging or concave characteristic of the entrance of the  $x$ -waves. The local convergence, temporal size independence, path lines, and  $x$ -velocity profile plots are for the  $2\Lambda_y$   $xz$ -plane. This plane exhibits a  $y$ -convex geometry. As mentioned in the technical literature [16, 22], convex and concave wall geometries affect flow patterns in a different way.

In the two previous paragraphs, the different effects of the entrance ( $x$ -concave wall) and middle ( $x$ -convex wall) of the channel  $x$ -waves were described. The  $x$ -concave wall generates no recirculation at the inlet because of the converging

flow before the entrance. However, the  $x$ -convex wall after the entrance generates recirculation because of the diverging flow after the entrance. Similar effects are expected of the  $y$ -convex or  $y$ -concave geometries, although to a lesser degree because the main flow is in the  $xz$ -plane. A comparison of the flow pattern between the  $2A_y$  and  $1.5A_y$   $xz$ -planes (henceforth referred to as Planes A and B, respectively) is of particular interest because the  $2A_y$   $xz$ -plane exhibits a  $y$ -convex geometry while the  $1.5A_y$   $xz$ -plane exhibits a  $y$ -concave geometry. As mentioned in [16], these two planes are far from the side walls to avoid any significant effects from the hydrodynamic  $y$ -boundary layer caused by such walls ( $A_y = 2.65\delta_y$  at the exit of the channel). Although the local convergence, temporal size independence, pathlines, and  $x$ -velocity profile plots are not shown for Plane B, the flow pattern behavior explained a few paragraphs above for Plane A holds for Plane B. The main difference between the flow patterns for Planes A and B is only the size of the recirculations.

Figures 11 and 12 show the detachment point ( $R_{st}$ ) location and the recirculation length ( $R_L$ ) as a function of time and  $x$ -wave for Planes A and B. Few differences can be noticed for the detachment point among these planes: the most

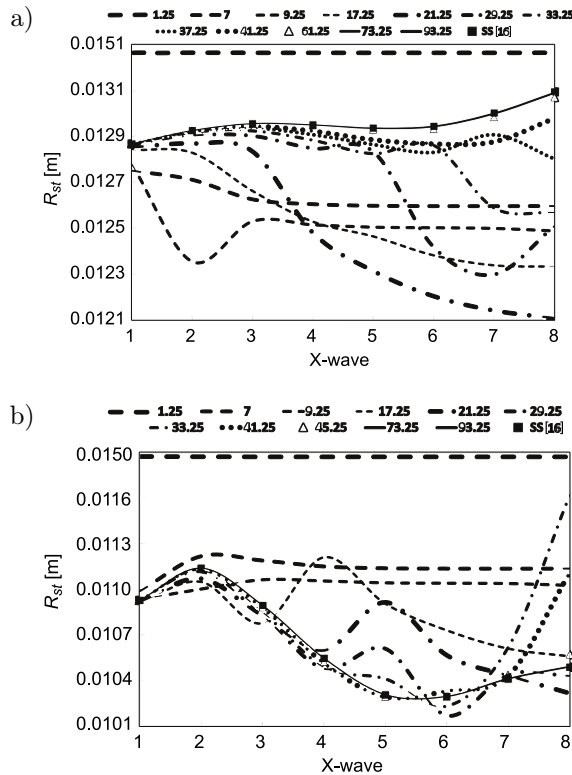


FIG. 11. Distance from  $x$ -wave inlet at which detachment occurs for: a)  $y = 1.5A_y$  and b)  $y = 2A_y$ ;  $Re = 600$  and  $180^\circ$  model.

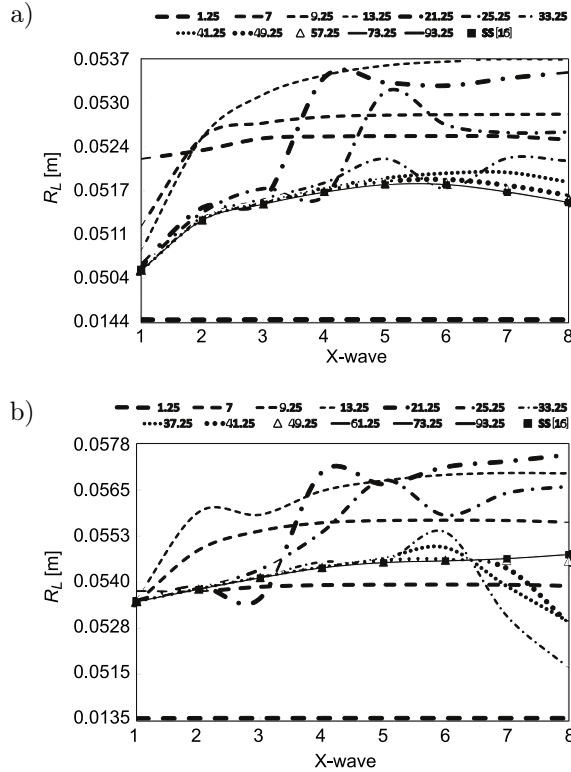


FIG. 12. Recirculation length for: a)  $y = 1.5\lambda_y$  and b)  $y = 2\lambda_y$ ;  $Re = 600$  and  $180^\circ$  model.

remarkable difference is that the detachment distances are longer for Plane B (0.0121–0.0131 m) than those for Plane A (0.0101–0.0116 m), the curves approach the steady state from below for Plane B and from above for Plane A, and the steady state is practically achieved at 61.25 s for Plane B and at 45.25 s for Plane A. From these differences, it can be inferred that  $y$ -concave geometries inhibit fluid detachment (higher detachment points) and steady state achievement (longer time to reach steady state). Two differences can be remarked in the recirculation length between planes: the most important difference is that the range of recirculation length values is smaller for Plane B (0.0504–0.0537 m) than those for Plane A (0.0515–0.0578 m), and the steady state is practically achieved at 57.25 s for Plane B and at 49.25 s for Plane A. Again, it can be inferred that  $y$ -concave geometries disfavor recirculation formation (smaller recirculation length) and steady state achievement (longer time to reach steady state). For both planes, the temporal development of the flow is significantly close to the inlet for small time values (observe the non-horizontal looking curve for the first three  $x$ -waves at 7 and 9.25 s in Figs 11 and 12). As time advances, this flow's temporal development at the inlet reaches a steady state, while it begins to affect

the waves closer to the outlet of the channel (see the relatively small differences of the curves shape for the first three  $x$ -waves and the non-horizontal like curve behavior for the rest of the  $x$ -waves after 21.25 s in Figs 11 and 12); finally, the flow temporal development achieves the steady state all over the channel at a prolonged time (it can be observed that the curves have practically achieved steady state after 49.25 s in Figs 11 and 12).

### 3.2. Transient flow pattern: $0^\circ$ model

The converged scale residuals are depicted in Fig. 13a for a transient analysis performed for a total elapsed time of 93.25 s (the steady state has been well established at such time). 193 unsteady solutions were obtained using a time increment of 0.25 s for the first 181 solutions, and 4 s for the final 12 solutions. A global convergence was considered to be achieved when the velocity and continuity residuals achieved a value in the order of  $10^{-6}$ . Every time a solution was determined for a particular time, the scale residuals increased to a high initial value that kept decreasing until convergence was achieved (i.e., a decrease of

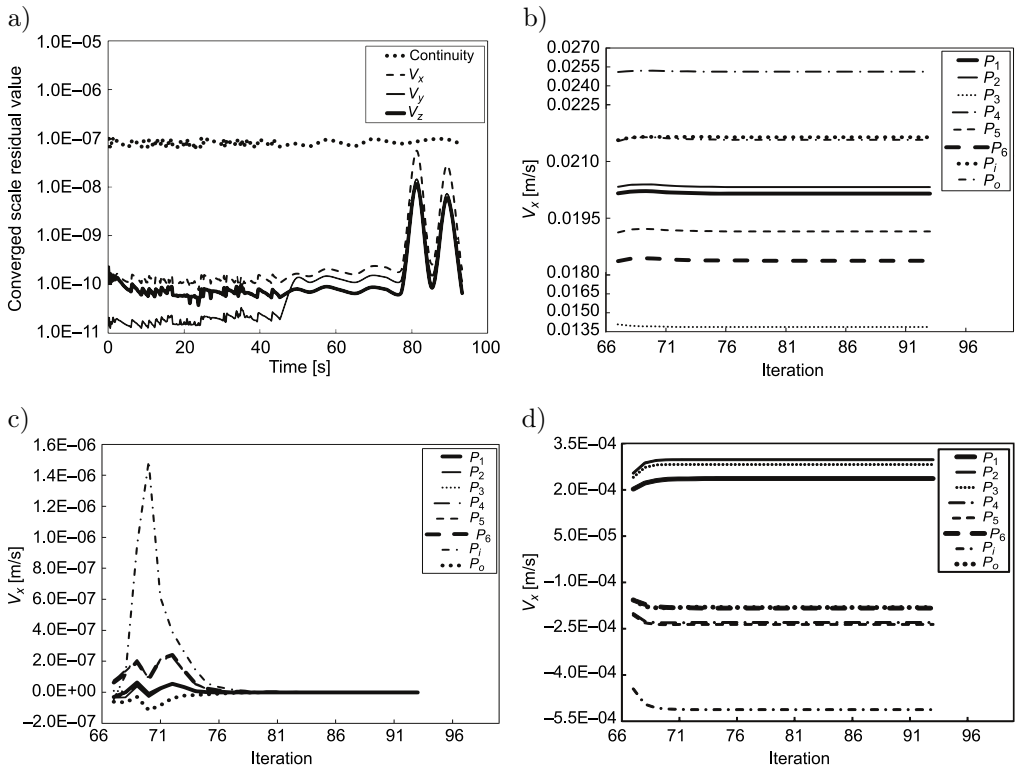


FIG. 13. Convergence studies: a) global, b) local  $V_x$ , c) local  $V_y$ , and d) local  $V_z$ .  $2\lambda_y$   $xz$ -plane and  $0^\circ$  model. Local convergence is shown for 29.25 s.

six significant digits was reached). The local convergence was verified for every temporal solution in the selected locations of the channel depicted in Fig. 3b. For the sake of brevity, only the local convergence plots for 0.75 s are presented in Figs 13b to 13d. In these figures, it can be observed that the local velocities attained quite a constant value (the absolute percentage of change between consecutive iterative velocities in the horizontal line region was calculated to be well below 0.1%) for a considerable amount of iterations (i.e., local convergence has been attained).

Next, a temporal size-independent study was performed by considering four different time steps (0.25, 0.5, 1, and 2 s). The local velocities obtained for selected locations after 2 s were compared among the different time steps (see Fig. 14). From this figure, it can be observed that the difference among converged velocities is not significant (the curves are practically straight lines for  $V_x$  and  $V_y$  local velocities). The curves for  $V_z$  are a little more variable, but the differences in magnitude between consecutive time steps are small. Moreover, the velocity difference between those velocities for the first two time steps (0.25 and 0.5 s)

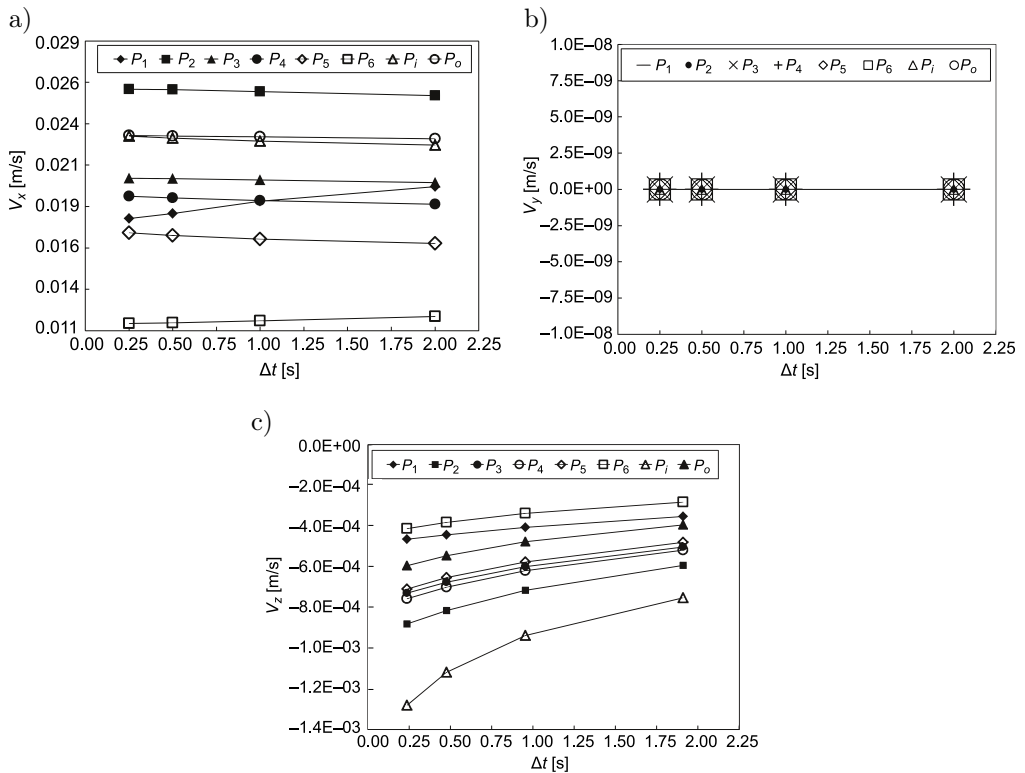


FIG. 14. Temporal size independence study for: a)  $V_x$ , b)  $V_y$ , and c)  $V_z$ ;  $2A_y$   $xz$ -plane and  $0^\circ$  model.

is always the smallest. Maximum percentages of difference around 1.7% would be achieved between 0.25 and 0.5 s time steps, if percentages of difference were determined among the converged total velocities for consecutive time steps. As with the  $180^\circ$  model, it can be inferred that converged velocities for time steps below 0.25 s will show no significant differences with those determined for a time step of 0.25 s. Consequently, several solutions were obtained for a time step of 0.25 s until the steady state was considered to be achieved. For the few several initial solutions, the time step of 0.25 s was used, but it was changed to 4 s after a quasi-steady state was observed in order to completely corroborate the steady state at much bigger values of time.

Figure 15 shows the few selected path lines exemplifying the temporal progress of the recirculation formation. At early times (check the path lines for 3 s), it can be clearly seen that the detachment point starts relatively far from the  $x$ -wave inlet, the reattachment point begins closer to the entrance than for longer times, and the size of the recirculation is quite small. At moderate times (see the path lines for 5.25 s), the size of the recirculation is considerably larger and closer to the main flow, the reattachment point is further away from the  $x$ -wave inlet when compared to the case of earlier times, and the detachment point moves moderately closer to the  $x$ -wave inlet. As time evolves, the size of the recirculation keeps growing, the reattachment point keeps advancing farther from the  $x$ -wave inlet, and the detachment point keeps moving slowly to the  $x$ -wave inlet. These evolutions on the characteristics of the recirculation diminish gradually until no changes are seen (i.e., steady state has been achieved). As with the  $180^\circ$  model, the steady state is accomplished faster at  $x$ -waves closer to the inlet ( $x$ -wave

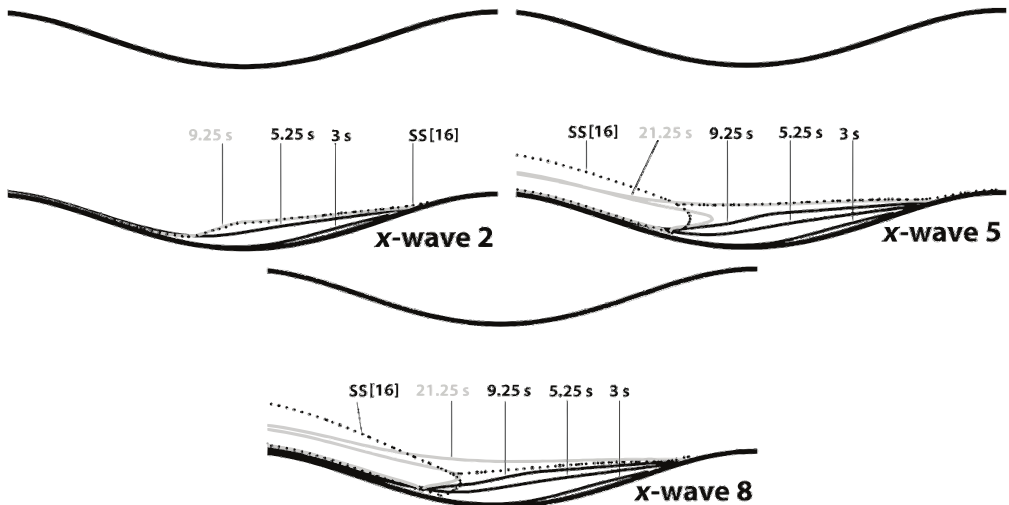


FIG. 15. Path lines showing the recirculation behavior as the fluid progresses downstream and time advances.  $2A_y$   $xz$ -plane and  $0^\circ$  model. The main flow direction is from right to left.

2 reached it around 9.25 s, while  $x$ -wave 5 and  $x$ -wave 8 will reach it beyond 21.25 s). At  $x$ -waves numbers above  $x$ -wave 2 and long enough times, the fluid detaching from the wall does not reattach anymore and joins the main flow (“open recirculations” are being developed), while the reattachment point is a point at which fluid joins from other planes and follows an upstream path (forming part of the “open recirculation”) or a downstream path (joining the main flow). Such “open recirculations” appearing as the flow approaches the channel outlet were well documented in [16] in the complete steady state analysis of such corrugated plates. A few differences can be noticed between the  $180^\circ$  and  $0^\circ$  models: the recirculations appear at longer times and are smaller in the  $0^\circ$  model than those in the  $180^\circ$  model, and the flow pattern in the  $0^\circ$  model achieves a steady state faster than that of the  $180^\circ$  model (compare Figs 6 and 15). The first difference is caused by the fluid trying to follow the parallel path in the  $0^\circ$  model (inhibiting detachment) and the second difference is most likely caused by the same reason. The growing interaction between the secondary flow and the main flow, as time advances and as the channel outlet is approached, is a direct consequence of the flow developing in space and time.

Figures 16 to 18 show the  $x$ -velocity profiles at different locations of the channel for selected times (these locations are at the bottom center of different  $x$ -waves and in the  $1.5A_y$   $xz$ -plane). By comparing  $x$ -velocity profiles over time for a given  $x$ -wave, it can be observed that the walls affect more the fluid at the center of the channel as time advances (i.e., temporal flow development). By comparing  $x$ -velocity profiles at different channel locations, it can be seen that the walls affect more the fluid at the center of the channel as the  $x$ -wave

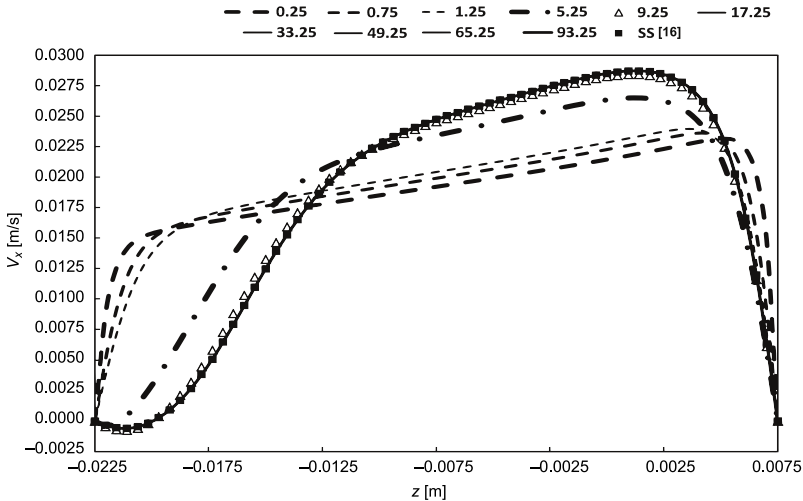


FIG. 16.  $V_x$  velocity profile as function of time for  $x = 1.5A_x$  and  $y = 1.5A_y$ ;  $Re = 600$ ,  $2A_y$   $xz$ -plane and  $0^\circ$  model.

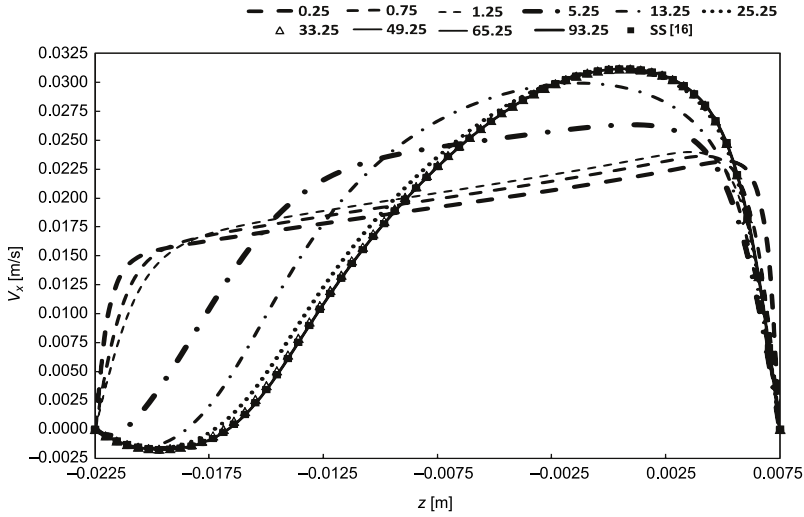


FIG. 17.  $V_x$  velocity profile as function of time for  $x = 4.5A_x$  and  $y = 1.5A_y$ ;  $Re = 600$ ,  $1.5A_y$   $xz$ -plane and  $0^\circ$  model.

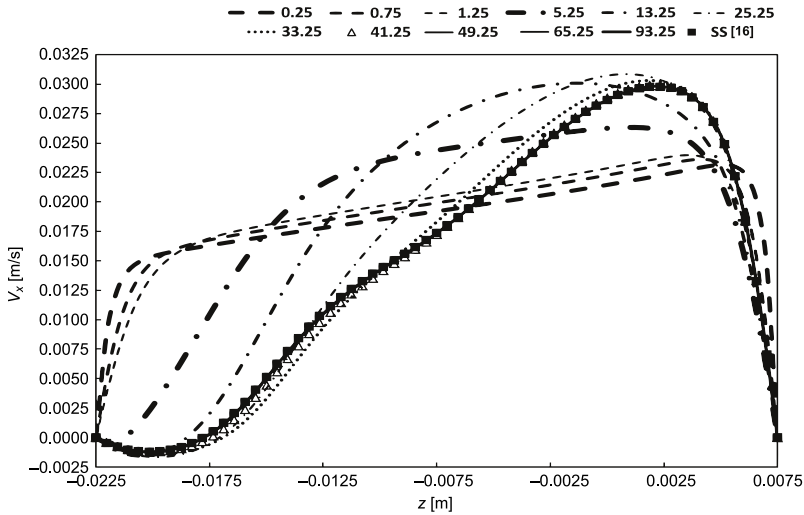


FIG. 18.  $V_x$  velocity profile as function of time for  $x = 7.5A_x$  and  $y = 1.5A_y$ ;  $Re = 600$ ,  $1.5A_y$   $xz$ -plane and  $0^\circ$  model.

increases (i.e., spatial flow development). Certainly, full development will be reached at long enough times and lengths. As seen in Figs 16 to 18, temporal flow development or steady state has been practically reached by the  $x$ -velocity profiles at 9.25 s, 33.25 s, and 49.25 s for  $x$ -waves 2, 5, and 8, respectively. As in the  $180^\circ$  model, this confirms that the steady state is attained faster at  $x$ -waves closer to the channel inlet.

Figure 19 shows the  $x$ -velocity profile over time for the entrance of  $x$ -wave 8. From this figure, it can be seen how the velocity profile reaches the steady state at about 45.25 s. Unlike the  $x$ -velocity profile at the center of the  $x$ -waves, this velocity profile shows the secondary flow at the top of the channel (the walls have an  $x$ -convex surface at the top and an  $x$ -concave surface at the bottom for this location). In other words, just before this location, the fluid is diverging (promoting separation) at the top and converging (inhibiting separation) at the bottom. The local convergence, temporal size independence, pathlines, and  $x$ -velocity profile plots are for the  $1.5A_y$   $xz$ -plane. This plane exhibits a  $y$ -convex geometry. As in the previous  $180^\circ$  model, the effects of the  $y$ -convex or  $y$ -concave geometries of the corrugated plates were analyzed. A comparison of the flow pattern between the  $2A_y$  and  $1.5A_y$   $xz$ -planes (i.e., Planes A and B, respectively) was performed. The  $2A_y$   $xz$ -plane exhibits a  $y$ -concave geometry while the  $1.5A_y$   $xz$ -plane a  $y$ -convex geometry. The local convergence, temporal size independence, pathlines, and  $x$ -velocity profile plots are not shown for Plane A, but the flow pattern behavior explained a few paragraphs above for Plane B holds for Plane A. Only the size of the recirculations is different between the flow patterns for Planes A and B.

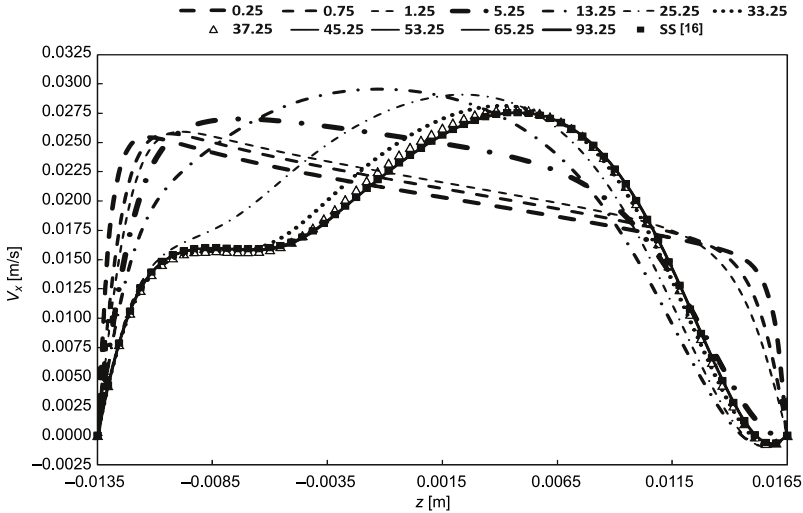


FIG. 19.  $V_x$  velocity profile as function of time for  $x = 7A_x$  and  $y = 1.5A_y$ ;  $Re = 600$ ,  $1.5A_y$   $xz$ -plane and  $0^\circ$  model.

Figures 20 and 21 show the detachment point ( $R_{st}$ ) location and the recirculation length ( $R_L$ ) as a function of time and  $x$ -wave for Planes A and B. Two main differences can be noticed for the detachment point among planes: the detachment values are higher for Plane A (0.017–0.027 m) than those for Plane B (0.010–0.020 m), and steady state is practically achieved at 37.25 s

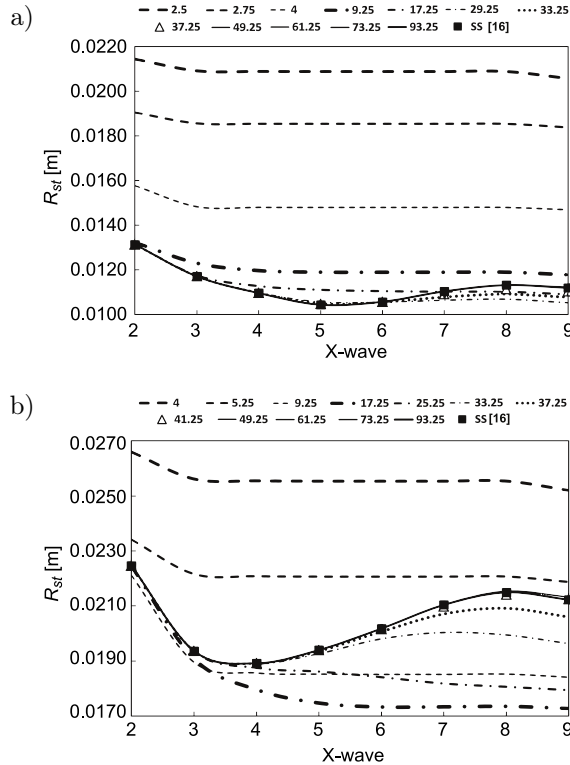


FIG. 20. Distance from  $x$ -wave inlet at which detachment occurs for: a)  $y = 1.5\Delta y$  and b)  $y = 2\Delta y$ ;  $Re = 600$  and  $0^\circ$  model.

for Plane B and at 41.25 s for Plane A. From these two differences, it can be inferred, in agreement with the  $180^\circ$  model, that  $y$ -concave geometries inhibit fluid detachment (higher detachment values) and steady state achievement (longer time to reach a steady state). Two differences can be mentioned for the recirculation length between planes: the recirculation length values are larger for Plane B (0.0269–0.0488 m) than those for Plane A (0.0073–0.0365 m); and steady state is practically attained at 37.25 s for Plane B and at 41.25 s for Plane A. Once more, it can be corroborated that  $y$ -concave geometries do not favor recirculation formation (smaller recirculation lengths) and steady state achievement (higher times for steady state). As in the  $180^\circ$  model, the flow temporal development is significantly closer to the inlet for small time values (e.g., this can be clearly seen in the non-horizontal looking curve for the first three  $x$ -waves at 4, 5.25, and 9.25 s in Fig. 20b). As time advances, this temporal development of the flow at the inlet reaches a steady state, while it begins to affect the waves closer to the outlet of the channel (clearly seen in the relatively small differences of the curves shapes for the first three  $x$ -waves and the non-horizontal like curve behavior for the rest of the  $x$ -waves after 25.25 s in Fig. 20b). Finally, the

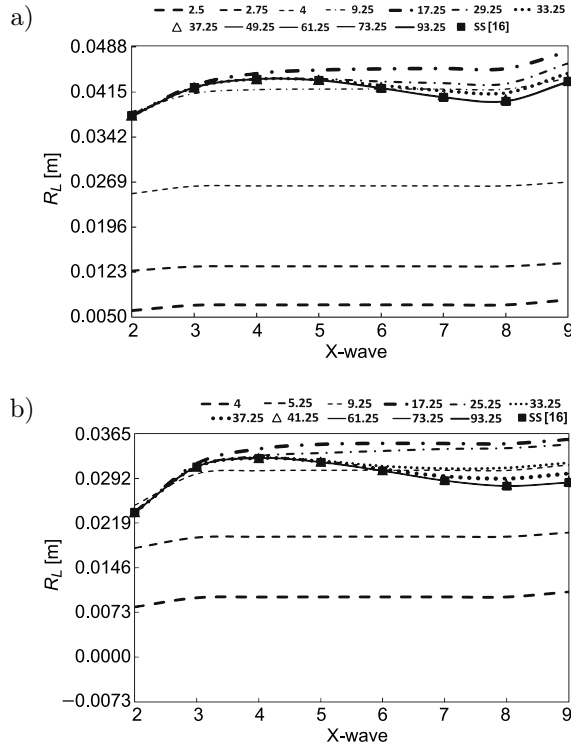


FIG. 21. Recirculation length for: a)  $y = 1.5A_y$  and b)  $y = 2A_y$ ;  $Re = 600$  and  $0^\circ$  model.

temporal development of the flow achieves the steady state all over the channel at a prolonged time (it can be corroborated that the curves have practically achieved a steady state after 41.25 s in Figs 20 and 21).

#### 4. CONCLUSIONS

A detailed numerical study of the unsteady laminar flow pattern between two corrugated plates with an egg-carton configuration was developed. The numerical study was performed for three Reynolds numbers (200, 400, and 600). Two phase angles ( $180^\circ$  and  $0^\circ$ ) between the two corrugated plates were studied. The temporal and spatial development of flow particle paths, detachment point, and the recirculation length were illustrated and discussed for both the  $180^\circ$  and  $0^\circ$  egg-carton corrugated channels. The effects of the geometry on the flow patterns were the same as those described in [16]: for both phase angles, “closed recirculations” diminished in size downstream the channel and finally disappeared becoming “open recirculations” because of spatial flow development. The recirculations in the  $180^\circ$  egg-carton corrugated plates were  $z$ -symmetric with respect

to the center of the channel, but the recirculations for the  $0^\circ$  egg-carton corrugated plates were not. "Closed recirculations" in the  $0^\circ$  egg-carton corrugated plates were smaller and became "open recirculations" earlier than those of the  $180^\circ$  egg-carton corrugated plates, and, in both phase angle models, convex geometries on the transversal direction favored detachment while concave geometries inhibited it. As in previous experimental [13] and numerical investigations [16], increments of Reynolds number were found to favor recirculation growth and early flow detachment. For both phase angles, the transient development effects were as follows: steady state was achieved faster in waves closer to the entrance of the channel. As time advanced, spatial flow development advanced toward the outlet of the channel, and  $y$ -concave geometries inhibited steady state achievement. The recirculations appeared at larger times and were smaller in the  $0^\circ$  model than those in the  $180^\circ$  model, and the flow pattern in the  $0^\circ$  model achieved a steady state faster than that of the  $180^\circ$  model. These are clear consequences of the geometry influence on the transient development of the flow patterns. The flow patterns behavior achieved at the steady state was found to agree with the one obtained in [16].

All of the unsteady effects on the flow patterns mentioned in the paragraph above are natural consequences of a flow developing in time. On the other hand, no clear evidence of vortices that seem to travel from wave inlet to wave outlet by rolling on the surface of the plates ("rolling vortices") was observed. It can be concluded that such unsteady flow features observed in previous experimental studies [13] might be a consequence of an unavoidable small variation of the experimental flow velocity generating a pulsating flow and not a consequence of a flow developing on time with a constant channel inlet velocity. To corroborate this, future detailed unsteady analyses should be performed by varying the velocity at the entrance of the channel over time and creating a pulsating flow. Such temporal variation should consider the unsteady analysis results of this research to assess completely the effects of small variations of inlet velocities in the flow patterns between two egg-carton corrugated plates. Finally, it can be concluded that this unsteady numerical analysis was very adequate in presenting the temporal processes accompanying the flow to achieve most of the flow patterns observed in [13, 16].

#### ACKNOWLEDGMENTS

This work was supported by The Chinese Natural Science Foundation of the Henan Province [grant numbers 182300410169, 182102210201] and by The Support Project of Scientific and Technological Innovation Talents of Universities in Henan Province [19HASTIT023].

## REFERENCES

1. AMMAR H., OULD EL MOCTAR A., GARNIER B., PEERHOSSAINI H., Flow pulsation and geometry effects on mixing of two miscible fluids in microchannels, *ASME Journal of Fluids Engineering*, **136**(12): 121101, 9 pages, 2014, doi: 10.1115/1.4027550
2. ÜNAL E., AHN H., SORGUVEN E., Experimental investigation on flows in a corrugated channel, *ASME Journal of Fluids Engineering*, **138**(7): 070908, 8 pages, 2016, doi: 10.1115/1.4032754
3. KARAMI M., SHIRANI E., JARRAHI M., PEERHOSSAINI H., Mixing by time-dependent orbits in spatiotemporal chaotic advection, *ASME Journal of Fluids Engineering*, **137**(1): 011201, 13 pages, 2015, doi: 10.1115/1.4027588
4. TAKABI B., SALEHI S., Augmentation of the heat transfer performance of a sinusoidal corrugated enclosure by employing hybrid nanofluid, *Advances in Mechanical Engineering*, **6**: 1–16, 2014, doi: 10.1155/2014/147059
5. HEMIDA H.N., SABRY M.N., ABDEL-RAHIM A., MANSOUR H., Theoretical analysis of heat transfer in laminar pulsating flow, *International Journal of Heat and Mass Transfer*, **45**(8): 1767–1780, 2002, doi: 10.1016/S0017-9310(01)00274-5.
6. KHANAFER K., AL-AZMI B., AL-SHAMMARI A., POP I., Mixed convection analysis of laminar pulsating flow and heat transfer over a backward-facing step, *International Journal of Heat and Mass Transfer*, **51**(25–26): 5785–5793, 2008, doi: 10.1016/j.ijheatmasstransfer.2008.04.060.
7. JAFARI M., FARHADI M., SEDIGHI K., Heat transfer enhancement in a corrugated channel using oscillating flow and nanoparticles: an Lbm approach, *Numerical Heat Transfer, Part A: Applications*, **65**(6): 601–626, 2014, doi: 10.1080/10407782.2013.836023.
8. OVIEDO-TOLENTINO F., ROMERO-MÉNDEZ R., HERNÁNDEZ-GUERRERO A., GIRÓN-PALOMARES B., Use of diverging or converging arrangement of plates for the control of chaotic mixing in symmetric sinusoidal plate channels, *Experimental Thermal and Fluid Science*, **33**(2): 208–214, 2009, doi: 10.1016/j.expthermflusci.2008.08.002.
9. OVIEDO-TOLENTINO F., ROMERO-MÉNDEZ R., HERNÁNDEZ-GUERRERO A., GIRÓN-PALOMARES B., Experimental study of fluid flow in the entrance of a sinusoidal channel, *International Journal of Heat and Fluid Flow*, **29**(5): 1233–1239, 2008, doi: 10.1016/j.ijheatfluidflow.2008.03.017.
10. RAMGADIA A.G., SAHA A.K., Characteristics of fully developed flow and heat transfer in channels with varying wall geometry, *Journal of Heat Transfer*, **136**(2): 021703, 15 pages, 2014, doi: 10.1115/1.4024552.
11. MAHMUD S., SADRUL ISLAM A., FERAZ C., Flow and heat transfer characteristics inside a wavy tube, *Heat and Mass Transfer*, **39**(5): 387–393, 2003, doi: 10.1007/s00231-002-0369-9.
12. ABROSHAN H., Numerical simulation of turbulent flow and heat transfer through sinusoidal ducts, *Heat and Mass Transfer*, **54**(7): 2045–2059, 2018, doi: 10.1007/s00231-018-2277-7.
13. GIRÓN-PALOMARES B., HERNÁNDEZ-GUERRERO A., ROMERO-MÉNDEZ R., OVIEDO-TOLENTINO F., An experimental analysis of the flow pattern in heat exchangers with an egg carton configuration (parallel, convergent and divergent cases), *International Journal of Heat and Fluid Flow*, **30**(1): 158–171, 2009, doi: 10.1016/j.ijheatfluidflow.2008.09.005.

14. SAWYERS D.R., SEN M., CHANG H.-C., Heat transfer enhancement in three-dimensional corrugated channel flow, *International Journal of Heat and Mass Transfer*, **41**(22): 3559–3573, 1998, doi: 10.1016/S0017-9310(98)00029-5.
15. RUSH T.A., NEWELL T.A., JACOBI A.M., An experimental study of flow and heat transfer in sinusoidal wavy passages, *International Journal of Heat and Mass Transfer*, **42**(9): 1541–1553, 1999, doi: 10.1016/S0017-9310(98)00264-6.
16. GIRON-PALOMARES B., HERNANDEZ-GUERRERO A., ROMERO-MENDEZ R., HE Q., A study of the flow patterns between two corrugated plates with an egg-carton configuration, *ASME Journal of Fluids Engineering*, **141**(2): 021104, 13 pages, 2019, doi: 10.1115/1.4040594.
17. ISSA R.I., AHMADI-BEFRUI B., BESHAY K.R., GOSMAN A.D., Solution of the implicitly discretised reacting flow equations by operator-splitting, *Journal of Computational Physics*, **93**(2): 388–410, 1991, doi: 10.1016/0021-9991(91)90191-M.
18. FERZIGER J.H., PERIC M., *Computational Methods for Fluid Dynamics*, Springer, Berlin Heidelberg, New York, 2002.
19. ANDERSSON B., ANDERSSON R., HÅKANSSON L., MORTENSEN M., SUDIYO R., VAN WACHEM B., *Computational Fluid Dynamics for Engineers*, Cambridge University Press, Cambridge, 2011.
20. CHEN Z.J., PRZEKWAŚ A.J., A coupled pressure-based computational method for incompressible/compressible flows, *Journal of Computational Physics*, **229**(24): 9150–9165, 2010, doi: 10.1016/j.jcp.2010.08.029.
21. KAYA F., KARAGOZ I., Performance analysis of numerical schemes in highly swirling turbulent flows in cyclones, *Current Science*, **94**(10): 1273–1278, 2008.
22. KUNDU P.K., COHEN I.M., *Fluid Mechanics*, Academic Press, Burlington, MA, 2008.

*Received September 23, 2019; accepted version December 11, 2020.*

---

*Published on Creative Common licence CC BY-SA 4.0*

